Dynamics of Hypoid Gear Transmission With Nonlinear Time-Varying Mesh Characteristics

Yuping Cheng
Mem. ASME
Ford Motor Company,
Livonia, MI 48150

Teik C. Lim
Associate Professor,
Mem. ASME
e-mail: teik.lim@uc.edu
Department of Mechanical, Industrial & Nuclear Engineering,
The University of Cincinnati
Cincinnati, OH 45221-0072

The coupled translation-rotation vibratory response of hypoid geared rotor system due to loaded transmission error excitation is studied by employing a generalized 3-dimensional dynamic model. The formulation includes the effects of backlash nonlinearity as well as time-dependent mesh position and line-of-action vectors. Its mesh coupling is derived from a quasi-static, 3-dimensional, loaded tooth contact analysis model that accounts for the precise gear geometry and profile modifications. The numerical simulations show significant tooth separation and occurrence of multi-jump phenomenon in the predicted response spectra under certain lightly loaded operating conditions. Also, resonant modes contributing to the response spectra are identified, and cases with super-harmonics are illustrated. The computational results are then analyzed to quantify the extent of non-linear and time-varying factors. [DOI: 10.1115/1.1564064]

1 Introduction

It is generally accepted that the gear kinematic transmission error is the primary source of vibratory energy excitation that produces tonal noise problems in geared applications including hypoid gear set used in automotive and aerospace drive trains. Extensive studies have been performed to synthesize machine tool and cutter settings in order to achieve the desired tooth profiles and contact patterns that minimize transmission errors [1–6]. However, very few studies on the system dynamic aspect of non-parallel gearing have been conducted. From the gear literature, only a few analytical investigations [7–11] on hypoid gear vibrations were found. On the other hand, the dynamics of parallel axis gears have been investigated extensively [12–19]. Of the few studies that exist on hypoid gear dynamics, many actually ignored the direct excitation of transmission error (TE) and/or did not define the mesh coupling explicitly. Most of these models essentially rely on overly simplified mesh force vector representations. For instance, the hypoid gear mesh model suggested by Donley et al. [20] for use in the context of performing linear time-invariant dynamic finite element calculations was based on a bevel gear mesh equivalence theory. More recently, Cheng and Lim [21–23] proposed a more sophisticated mesh coupling formulation derived from exact gear geometry for both spiral bevel and hypoid gears, and applied the resulting linear time-invariant (LTI) dynamic model to study drive train torsion and translation vibration responses.

Nonlinear vibration work on spur or helical gears in which gear backlash is present has been extensively studied by Özgüven and Houser [12], Kahraman et al. [14–16], Hochmann [24], and many others. In these investigations the gear contact position and line-of-action are assumed time-invariant. While this treatment may be reasonable due to the nature of kinematics in these types of gear pairs and in consideration of the small out-of-plane gear motion, it is not directly applicable to hypoid gears. This is because each point on the hypoid tooth contact areas traces a curvilinear path, as opposed to a nearly straight line in spur or helical gear case. Furthermore, the surface curvatures of hypoid gear teeth are significantly more complex. At the same time, the friction generated at the mesh interface could produce oblique internal dynamic forces and moment excitations on the gear members, even though not as significant as other types of gears since the relative sliding motion between the mating gear teeth is more uniform and does not reverse direction as the contact area crosses the mean pitch point. It may be pointed out that the effect of friction was also previously discussed by Hochmann [24] and Lida et al. [25] for parallel axis gears, and Handschuh and Kicher [26] for spiral bevel gears.

In the present study, a multi-degree-of-freedom, nonlinear time-varying (NLTV) lumped parameter dynamic model of the hypoid gear pair with torsional and translational effects is formulated. The model includes gear backlash, constant coefficient of friction, and time-dependent mesh position and effective line-of-action. Although the level of unloaded kinematic transmission error has been shown to be directly related to the severity of gear noise problem in numerous examples, the loaded transmission error (LTE) is believed to be better correlated to gear whine. This is due to the effects of tooth deflection and load sharing phenomena on transmission error [12,13,27,28]. Accordingly, in our analysis the loaded transmission error is formulated and incorporated into the dynamical equations of motions as the excitation source. In order to obtain the time-varying characteristics affecting mesh line-of-action, mesh position and load dependent mesh stiffness, a unique mesh generator is first employed to generate the theoretical tooth geometry from manufacture settings for a specific set of hypoid gear design [1–4,23,29]. The gear mesh parameters needed for the model are then determined by applying an existing loaded tooth contact analysis program [30,31], which is based on the finite element and surface integral methods. The program is essentially used to perform the quasi-static calculations needed to construct the nature of the gear mesh over one tooth-to-tooth cycle in discrete steps of angular positions. Finally, an efficient numerical solver based on the 5/6th order Runge-Kutta integration routine with adaptive size is used to compute the dynamic response due to loaded transmission error excitation. The resonant modes contributing to the response spectra are also identified, and the effects of non-linear and time-varying factors are quantified.

2 Gear Mesh Model

The derivation of the non-linear time-varying gear mesh model begins by performing a series of quasi-static, 3-dimensional tooth

Contributed by the Power Transmission and Gearing Committee for publication in the JOURNAL OF MECHANICAL DESIGN. Manuscript received July 2001; revised July 2002. Associate Editor: R. F. Handschuh.

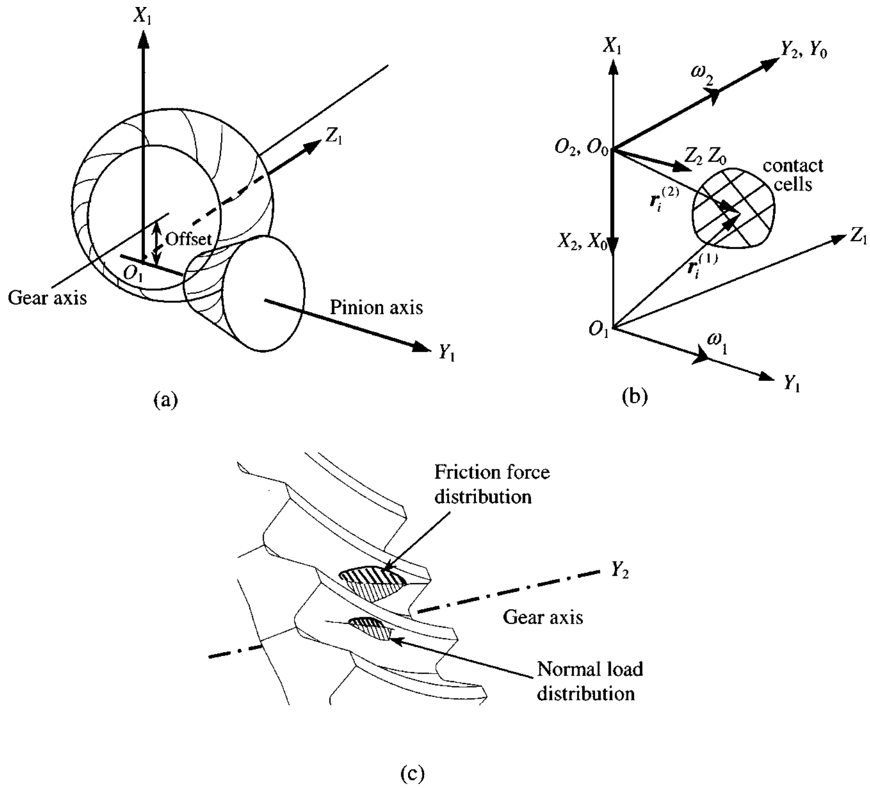

Fig. 1 Illustrations of (*a*) hypoid gear setup, (*b*) contact cells and three coordinate systems denoted by S_0, S_1 and S_2, and (*c*) load distributions on the tooth surface for a specific gear angular position

contact analysis using the Contact Analysis Program Package (CAPP) mentioned above. The program combines the finite element method and surface integral, and employs a Simplex type algorithm to simulate the elastic gear tooth contact engagement problem. The mesh point, stiffness, line-of-action, loaded transmission error, and normal and friction load distributions at discrete angular positions over one mesh cycle are computed. For a specific gear angular position, the contact areas of the gear teeth are discretized into groups of finite cells with uniform properties, as shown in Fig. 1. The local compliance between a pair of finite cells i and j, denoted by c_{ij}, is a function of the spatial dimensions, gear tooth meshing position and applied mean torque. The position vector of each contact cell i in the coordinate system S_l represented by X_l, Y_l and Z_l axes, $l=1$ (pinion) or 2 (gear), is $\mathbf{r}_i^{(l)}=\{x_i^{(l)}\ y_i^{(l)}\ z_i^{(l)}\}^T$, while the unit normal vector is given by $\mathbf{n}_i^{(l)}=\{n_{ix}^{(l)}, n_{iy}^{(l)}, n_{iz}^{(l)}\}^T$. The projection of the unit normal vector into the tangential direction of the gear rotational motion relative to S_l can be expressed as

$$\lambda_{ix}^{(l)}=\mathbf{n}_i^{(l)}\cdot(\mathbf{i}^{(l)}\times\mathbf{r}_i^{(l)}),\quad \lambda_{iy}^{(l)}=\mathbf{n}_i^{(l)}\cdot(\mathbf{j}^{(l)}\times\mathbf{r}_i^{(l)}),$$
$$\lambda_{iz}^{(l)}=\mathbf{n}_i^{(l)}\cdot(\mathbf{k}^{(l)}\times\mathbf{r}_i^{(l)}), \tag{1}$$

where $\mathbf{i}^{(l)}$, $\mathbf{j}^{(l)}$ and $\mathbf{k}^{(l)}$ are the triad of unit vectors that define the axes of S_l. Hence, the directional cosine of each cell i clearly depends on the gear geometry and its actual angular position. Here, the mesh parameter $\lambda_{iu}^{(l)}$ $(u=x,y,z)$ is referred to as the directional rotation radius about the respective u-axis, which qualitatively relates to the tangential force component at the contact point i per unit normal force along $n_i^{(l)}$. The relative sliding velocity vector $\boldsymbol{\nu}_i^{(12)}$ with respect to the coordinate system S_0, which is identical to S_2, may be transformed into a representation with respect to the local coordinate system S_l by $\boldsymbol{\nu}_i^{(l)}=[M_{l0}]\cdot\boldsymbol{\nu}_i^{(12)}=\{\nu_{ix}^{(l)}, \nu_{iy}^{(l)}, \nu_{iz}^{(l)}\}^T$, where $[M_{l0}]$ is the coordinate transformation matrix between S_O and S_l. Projection of the relative sliding velocity vector in the tangential direction of the gear rotational motion relative to X_l, Y_l and Z_l axes can be shown to be

$$\tau_{ix}^{(l)}=\nu_{iz}^{(l)}y_i^{(l)}-\nu_{iy}^{(l)}z_i^{(l)},\quad \tau_{iy}^{(l)}=\nu_{ix}^{(l)}z_i^{(l)}-\nu_{ix}^{(l)}x_i^{(l)},$$
$$\tau_{iy}^{(l)}=\nu_{ix}^{(l)}z_i^{(l)}-\nu_{ix}^{(l)}x_i^{(l)}. \tag{2}$$

Here, $\boldsymbol{\tau}_{iu}^{(l)}$ relates to the tangential friction force component at contact point i per unit friction force in the sliding direction $\nu_i^{(l)}$.

The loaded transmission error is typically the net result of both tooth profile errors, and tooth deflections due to base rotation, bending, shearing and contact deformation. Suppose the pinion and gear contact regions are divided into N_c number of finite cells as depicted in Fig. 1(*b*), which is directly dependent on transmitted load and angular position. Since the instantaneous rotations of all simultaneously contacting cells are the same under load due to load sharing compatibility [27–30], the following expression for the equilibrium state of gear relative rotation, which is identical to the LTE of the pinion assuming stationary gear, can be derived as

$$\Delta\theta_L=\frac{T_1-(\{\boldsymbol{\Lambda}_1\}-\mu\{\mathbf{T}_1\})[C_\delta]^{-1}\{\mathbf{E}_0\}^T}{(\{\boldsymbol{\Lambda}_1\}-\mu\{\mathbf{T}_1\})[C_\delta]^{-1}\{\boldsymbol{\Lambda}_1\}^T}, \tag{3}$$

where T_1 is the mean torque applied to the pinion, μ is the friction coefficient, $\{\mathbf{T}_1\}=\{\tau_{1y}^{(l)}, \tau_{2y}^{(l)}, \ldots, \tau_{Ncy}^{(l)}\}$, and $\boldsymbol{\Lambda}_1=\{\lambda_{1y}^{(1)}\ \lambda_{2y}^{(1)}\ \ldots\ \lambda_{N_c y}^{(1)}\}$ is a vector of dimension N_c that represents the increase in separation between the mating gear teeth at each individual cell position due to the gear pair angular displacement $\Delta\boldsymbol{\theta}_L$. The compliance matrix $[C_\delta]$ contains the net displacements due to instantaneous normal and friction loads acting on all finite cells. The initial gear tooth separation vector is given by $\mathbf{E}_0=\{\varepsilon_{01}\ \ldots\ \varepsilon_{0N_c}\}$. It may be noted that due to the deflection of the gear teeth and effect of load sharing, the contact areas on the tooth surface are generally perturbed from its theoretical position. The LTE term in Eq. (3) denoted by $\Delta\theta_L$ is generally periodic with mesh frequency, and is a function of gear rotation position and applied load. It can be expressed in the Fourier expansion form as

$$\Delta\theta_L(\theta)=e_0+\sum_{r=1}^{n}(e_{rc}\cos(r\omega_m(\theta-\theta_0))+(e_{rs}\sin(r\omega_m(\theta-\theta_0)),$$

where ω_m is fundamental gear mesh frequency and θ_0 is initial position angle of the pinion.

3 Dynamic Formulation

Consider a generic drive train system comprising of a hypoid gear pair, a mechanical source and a load element as shown in Fig. 2. Each gear is modeled as a rigid conical body attached to a torsionally flexible shaft that is supported by compliant rolling element bearings represented by a set of discrete stiffness and damping elements [32]. Note that the nominal rotations of the pinion and gear are about Y_1 and Y_2 respectively. Furthermore, only the torsional coordinates of the driver θ_E and load θ_0 are modeled as their translation coordinates that are normally decoupled from those of the gears by use of flexible coupling design. The instantaneous nominal mesh vectors, including contact position and line-of-action, under the dynamic condition are assumed to be the same as those of the quasi-static condition for the identical angular position. In other words, we assume the normal and friction load distributions, and line-of-action are unperturbed by the vibratory response. This approach has also been used successfully in previous studies on parallel gear dynamics [13,14,18].

In order to improve computational efficiency and simplify the modeling process, the concept of equivalent mesh forces and moments will be used in the subsequent dynamic analysis. First, we must seek the equivalent mesh characteristics as a function of gear angular position based on the quasi-static results. To do so, consider the resultant normal force $F_{\delta u}^{(l)}$ and friction force $F_{fu}^{(l)}$ along the u-axis, where $u=x,y,z$, given by

$$F_{\delta u}^{(l)}=\sum_{i}^{Nc}\sum_{j}^{Nc} n_{iu}^{(l)}k_{ij}\delta_j=\mathbf{N}_u^{(l)}[C_\delta]^{-1}\mathbf{\Delta}_\delta=n_u^{(l)}W_0, \qquad (4a)$$

$$F_{fu}^{(l)}=\sum_{i}^{Nc}\sum_{j}^{Nc} \mu\nu_{iu}^{(l)}k_{ij}\delta_j=\mu\mathbf{V}_u^{(l)}[C_\delta]^{-1}\mathbf{\Delta}_\delta=\mu\nu_u^{(l)}W_0, \quad (4b)$$

where δ_j is the deformation of cell j, $\mathbf{\Delta}_\delta=\{\delta_1\delta_2\ldots\delta_{N_c}\}^T$, $\mathbf{N}_u^{(l)}=\{n_{1u}^{(l)}n_{2u}^{(l)}\ldots n_{N_cu}^{(l)}\}^T$, $\mathbf{V}_u^{(l)}=\{\nu_{1u}^{(l)}\nu_{2u}^{(l)}\ldots\nu_{N_cu}^{(l)}\}^T$, $[C_\delta]^{-1}\mathbf{\Delta}_\delta$ is the normal force acting at the gear mesh interface, and $W_0=T_1/(\lambda_y^{(1)}-\mu\tau_y^{(1)})$ is the equivalent normal load acting on the meshing teeth, which depends on the instantaneous transmission ratio and pinion angular position. Equation (4) gives the averaged normal and friction forces by summing the loads at every contact cells. Thus, $n_u^{(l)}$ and $\nu_u^{(l)}$ are the equivalent normal and frictional force vectors. Similarly, the resultant moments contributed by the normal and friction forces about the u-axis are

$$T_{\delta u}^{(l)}=\sum_{i}^{Nc}\sum_{j}^{Nc}\lambda_i^{(l)}k_{ij}\delta_j=\mathbf{\Lambda}_u^{(l)}[C_\delta]^{-1}\mathbf{\Delta}_\delta=\lambda_u^{(l)}W_0, \qquad (5a)$$

$$T_{fu}^{(l)}=\sum_{i}^{Nc}\sum_{j}^{Nc}\mu\tau_i^{(l)}k_{ij}\delta_j=\mu\mathbf{T}_u^{(l)}[C_\delta]^{-1}\mathbf{\Delta}_\delta=\mu\tau_u^{(l)}W_0, \quad (5b)$$

where $\mathbf{\Lambda}_u^{(l)}=\{\lambda_{1u}^{(l)}\lambda_{2u}^{(l)}\ldots\lambda_{N_cu}^{(l)}\}^T$ and $\mathbf{T}_u^{(l)}=\{\tau_{1u}^{(l)}\tau_{2u}^{(l)}\ldots\tau_{N_cu}^{(l)}\}^T$. The parameters $\boldsymbol{\lambda}_u^{(l)}$ and $\boldsymbol{\tau}_u^{(l)}$ are the equivalent directional rotation radii of the normal and friction forces respectively.

Next, consider the pinion and gear members whose motions are described by 3 orthogonal translation coordinates and the corresponding 3 other angular rotation coordinates given by $\mathbf{q}_l(t)=\{x_l\ y_l\ z_l\ \theta_{xl}\ \theta_{yl}\ \theta_{zl}\}^T$ where x_l, y_l and z_l are the translation terms, and θ_{xl}, θ_{yl} and θ_{zl} are the angular ones. Since the mesh and friction forces are determined under the quasi-static condition, the dynamic force and moment expressions can be further simplified by using the equivalent mesh vectors derived earlier. For gear member l, the equivalent normal and friction forces can be expressed as

$$F_{\delta u}^{(l)}=\sum_{i}^{Nc}\sum_{j}^{Nc} n_{iu}^{(l)}k_{ij}\delta_j=n_u^{(l)}k_m(\mathbf{h}^{(2)}\mathbf{q}_2-\mathbf{h}^{(1)}\mathbf{q}_1+\varepsilon_0), \quad (6a)$$

$$F_{fu}^{(l)}=\sum_{i}^{Nc}\sum_{j}^{Nc}\mu\nu_{iu}^{(l)}k_{ij}\delta_j=\mu\nu_u^{(l)}k_m(\mathbf{h}^{(2)}\mathbf{q}_2-\mathbf{h}^{(1)}\mathbf{q}_1+\varepsilon_0), \qquad (6b)$$

respectively, where ε_0 is the translation form of the unloaded kinematic transmission error in the direction of the line-of-action. Similarly, the equivalent dynamic moments due to normal and friction forces are

$$T_{\delta u}^{(l)}=\sum_{i}^{Nc}\sum_{j}^{Nc}\lambda_{iu}^{(l)}k_{ij}\delta_j=\lambda_u^{(l)}k_m(\mathbf{h}^{(2)}\mathbf{q}_2-\mathbf{h}^{(1)}\mathbf{q}_1+\varepsilon_0), \quad (7a)$$

$$T_{uf}^{(l)}=\sum_{i}^{Nc}\sum_{j}^{Nc}\mu\tau_{iu}^{(l)}k_{ij}\delta_j=\mu\tau_u^{(l)}k_m(\mathbf{h}^{(2)}\mathbf{q}_2-\mathbf{h}^{(1)}\mathbf{q}_1+\varepsilon_0), \qquad (7b)$$

respectively. In the above equations, $\mathbf{h}^{(l)}(t)=\{n_x^{(l)}n_y^{(l)}n_z^{(l)}\lambda_x^{(l)}\lambda_y^{(l)}\lambda_z^{(l)}\}$ denotes the mesh characteristic vector for a specific angular position and applied pinion torque. Thus, $\mathbf{h}^{(l)}$ is clearly time-varying and load-dependent. Under quasi-static condition, the scalar value of $(\mathbf{h}^{(2)}\mathbf{q}_2-\mathbf{h}^{(1)}\mathbf{q}_1)$ from the torsional gear contact analysis, in which $\mathbf{q}_1=\{\theta_1\}$ and $\mathbf{q}_2=\{\theta_2\}$, is essentially equivalent to the loaded transmission error e_L along the mesh force line-of-action direction. From Eqs. (5a) and (6a), the averaged mesh stiffness k_m can be shown to be $k_m=W_0/(\lambda_y^{(1)}\Delta\theta_L-\varepsilon_0)=W_o/(e_L-\varepsilon_0)$, where e_L is the translation form of LTE in the mesh force line-of-action direction. Similar expressions of the mesh stiffness are also used by Özgüven and Houser [13] and Blankenship and Singh [18]. Hence, the instantaneous k_m is a function of load, tooth errors, tooth modifications and gear rotation position. Accordingly, the equations of motion for the 14 degrees-of-freedom (DOF) system shown in Fig. 2 incorporating loaded transmission error term e_L are given by

$$I_E\ddot{\theta}_E+k_{t_1}(\theta_E-\theta_1)+c_{t_1}(\dot{\theta}_E-\dot{\theta}_1)=-T_1, \qquad (8a)$$

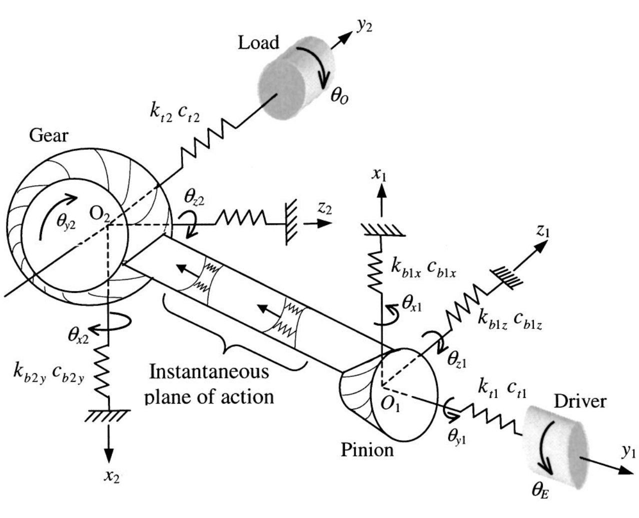

Fig. 2 A multi-degree-of-freedom lumped parameter model of a hypoid geared rotor system

$$[M_1]\{\ddot{\mathbf{q}}_1\}+(\mathbf{h}^{(1)^T}-\mu\mathbf{g}^{(1)^T})f(\delta_d-e_L)+[C_{1b}]\{\dot{\mathbf{q}}_1\}+[K_{1b}]\{\mathbf{q}_1\} = \{\mathbf{F}_{ext}^{(1)}\}, \tag{8b}$$

$$[M_2]\{\ddot{\mathbf{q}}_2\}-(\mathbf{h}^{(2)^T}+\mu\mathbf{g}^{(2)^T})f(\delta_d-e_L)+[C_{2b}]\{\dot{\mathbf{q}}_2\}+[K_{2b}]\{\mathbf{q}_2\} = \{\mathbf{F}_{ext}^{(2)}\}, \tag{8c}$$

$$I_O\ddot{\theta}_O+k_{t_2}(\theta_O-\theta_2)+c_{t_2}(\dot{\theta}_O-\dot{\theta}_2)=-T_2, \tag{8d}$$

where I_E and I_O are the mass moment of inertias of the driver and load, k_{t_1} and k_{t_2} are the torsional stiffnesses of the input and output shafts, c_{t_1} and c_{t_2} are the input and output shaft damping coefficients, T_1 and T_2 are the mean torques of the driver and load, $\{\mathbf{F}_{ext}^{(l)}\}$ is the external load vector acting on the gear member l, and the mass, stiffness and damping matrices of shaft-bearing components are given by $[M_l]$, $[K_{lb}]$ and $[C_{lb}]$ respectively. The damping terms shown explicitly here are viscous type and they represent the combined effects of all damping present in the system except for the mesh damping. For most practical transmissions, their values are typically equivalent to damping ratio of 0.01 to 0.02. The dynamic transmission error (DTE) is computed from $\delta_d=\mathbf{h}^{(1)}\{\mathbf{q}_1\}-\mathbf{h}^{(2)}\{\mathbf{q}_2\}$, while the time-varying, load-dependent vector for friction force is $\mathbf{g}^{(l)}(t) = \{\nu_x^{(l)}\nu_y^{(l)}\nu_z^{(l)}\tau_x^{(l)}\tau_y^{(l)}\tau_z^{(l)}\}$. In Eq. (8), the non-linear function $f(\delta_d-e_L)$ that describes the elastic mesh term is given by

$$f(\delta_d-e_L)=\begin{cases} W_0+k_m(t)\cdot(\delta_d-e_L)+c_m(\dot{\delta}_d-\dot{e}_L), \\ \qquad if\ \ W_d>0 \\ 0, \quad if\ \ W_d=0,-b_c<\delta_d<0, \\ W_0+k_m(t)\cdot(\delta_d-e_L+b_c)+c_m(\dot{\delta}_d-\dot{e}_L+b_c), \\ \qquad if\ \ W_d<0,\ \ \delta_d<-b_c \end{cases} \tag{9}$$

$$W_d=W_0+k_m(\delta_d-e_L)+c_m(\dot{\delta}_d-\dot{e}_L), \tag{10}$$

which is clearly dependent on the actual operating condition. Note that c_m in the above equation is the mesh damping defined for the losses from the tooth engagement process.

4 Computational Results

4.1 Procedure. Now consider a reduced order model that includes the pinion and gear rotation and translation coordinates, torsional compliances of the shafts, and shaft-bearing support stiffnesses. The pitch θ_{zl} and yaw θ_{xl} angular coordinates of both the pinion ($l=1$) and gear ($l=2$) are neglected as they were found to be unimportant in the earlier work by Cheng and Lim [22]. Furthermore, the formulation is transformed into a positive-definite system using $a_1(t)=\theta_1-\theta_E$, $a_2(t)=\lambda_y^{(2)}\theta_2-\lambda_y^{(1)}\theta_1$, and $a_3(t)=\theta_2-\theta_O$, which separates out the rigid body rotational mode and improves computational efficiency. The numerical solution of the proposed set of nonlinear, time-varying equations of motions governing the torsional and translational vibrations of the hypoid geared rotor system illustrated in Fig. 2 is obtained by applying the 5/6th order Runge-Kutta integration routine with adaptive time step capability. As part of the solution scheme, the second order differential form of Eq. (8) must be casted in the state-space domain generally given by $\dot{a}_i=f_i(a_1,a_2,\ldots,a_{18})$, where $i=1,2,\ldots,18$. The calculation generates the time domain steady-state vibratory response, which can be processed to provide either mesh frequency or order spectrum. A summary of the proposed computational approach is shown in Fig. 3. For comparison purpose, the corresponding linearized, time-averaged system model is also analyzed using the modal superposition method that has been presented in the earlier paper by Lim and Cheng [33]. The LTE calculated from the CAPP analysis is used as the primary excitation input into the proposed simulation process. Note that for a specific pinion/gear angular position, the dynamic load can be computed from Eq. (10), where numerically negative or zero dynamic load indicates the condition of tooth separation. When this detected, the possible occurrence of tooth backside collision is verified using Eq. (9). Occurrence of tooth backside collision leads to double-sided tooth impacts. If no backside collision is observed, then we simply get only single-sided tooth impacts. The former condition tends to produce multi-jump frequencies similar to those seen in gear rattle phenomenon. Note that the numerical results shown next assume no friction effect (i.e. $\mu=0$) to limit the scope of the present study, even though the proposed formulation established incorporates the mesh friction term explicitly.

4.2 Linear Time-Invariant. First, the loaded transmission error (LTE) and effective mesh stiffness k_m are computed for various torque load levels for the example case given in Table 1. The numerical result shows that the mean torque load applied to the pinion member tends to reduce the fundamental oscillation depth of the loaded transmission error, as depicted in Fig. 4(a). This is because larger tooth surface areas are in contact under higher torque load. Therefore, the fundamental mesh harmonic component of LTE decreases in magnitude with increasing torque load. This can be clearly seen in Figs. 4(b) and 4(c) that illustrate the Fourier coefficients of LTE for torque load levels of 113 Nm and 509 Nm respectively. That is why the higher harmonics, in particular the second order one appears more dominant at higher operating load. Likewise, the effect of mean torque load applied at the pinion member on averaged mesh stiffness of the hypoid gear pair is shown in Fig. 5. Here, it can be seen that k_m initially increases quite rapidly with increasing torque at lower load range but reaches an upper limit as load continues to rise beyond 500 Nm or so.

Next, the free vibration analysis assuming linear time-invariant mesh stiffness and force vector is performed. For the hypoid gear set defined in Table 1, three modal families are obtained: (i) out-of-phase gear torsional mesh coupled with translational motions of pinion and/or gear; (ii) in-phase gear torsional mesh coupled

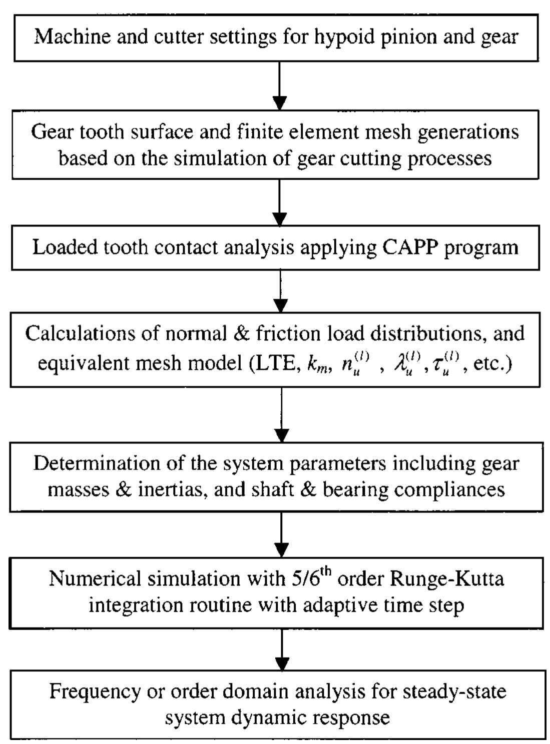

Fig. 3 Flowchart of the proposed computational approach

Table 1 Machine settings and gear design parameters for face-milled Gleason hypoid gear set

Gear data:	
Number of pinion teeth	10
Number of gear teeth	43
Gear face width (mm)	48
Gear face angle (radian)	1.2834
Gear root angle (radian)	1.2322
Gear addendum (mm)	3.41
Gear dedendum (mm)	10.42
Mean cone distance (mm)	152.14
Pinion offset (mm)	31.75
Pinion type	left-hand
Pinion machine and cutter settings:	
Cutter blade angle (radian)	0.3491
Machine center to back (mm)	−4.5847
Basic swivel angle (radian)	−0.7046
Basic cradle angle (radian)	1.0614
Sliding base (mm)	18.242
Ratio of roll	3.9936
Blank offset (mm)	24.542
Machine root angle (radian)	−0.0226
Point radius (mm)	108.450
Radial setting (mm)	118.513
Gear machine and cutter settings:	
Machine root angle (radian)	1.2287
Machine center to back (mm)	1.270
Horizontal setting (mm)	85.598
Vertical setting (mm)	96.177
Cutter blade angle (radian)	0.3927
Nominal radius (mm)	114.30
Point width (mm)	3.81
System Parameters:	
Pinion mass moment of inertia (kg-m^2)	8.3E−3
Pinion assembly mass (kg)	12.0
Driver mass moment of inertia (kg-m^2)	5.5E−3
Load mass moment of inertia (kg-m^2)	0.10
Gear assembly mass (kg)	49.5
Gear mass moment of inertia (kg-m^2)	0.52
Pinion shaft bending stiffness (Nm/rad)	1.0E6
Pinion shaft torsional stiffness (Nm/rad)	1.0E4
Gear shaft bending stiffness (Nm/rad)	8.0E6
Gear shaft torsional stiffness (Nm/rad)	5.0E5
Axial support stiffness (N/m)	1.0E8
Lateral support stiffness (N/m)	3.0E8

with translational motions of pinion and/or gear; and (iii) pure translation motions of pinion and/or gear member. The predicted modes and their corresponding natural frequencies are provided in Table 2 for three pinion mean torque loads. Modes 5 and 8 are pure translations that are basically decoupled from the mesh-coupling coordinate. Thus, their corresponding natural frequencies are essentially independent of the transmitted torque load or mesh stiffness. On the other hand, the natural frequencies of modes 7 and 9 with stronger gear mesh dependency vary slightly more with load due to change in effective mesh position and line-of-action.

4.3 Nonlinear Time-Varying (NLTV). The time-varying behavior of the hypoid gear pair is determined by the mesh characteristic vectors $\lambda_u^{(l)}$ and $n_u^{(l)}$ related to the normal force, and $\tau_u^{(l)}$ and $\nu_u^{(l)}$ associated with the friction force. The variations in these mesh characteristic vectors partly caused by the change in the number of tooth pairs in mesh as the gears rotate through one mesh cycle are greater for lighter torque and consequently lower for higher torque as shown in Fig. 6. Figure 7 shows the number of tooth pairs in contact varying periodically between 1 and 2. Note that the equivalent normal and friction force vectors vary more rapidly in the vicinity of the angular positions where the number of tooth pairs in contact changes. For the present hypoid

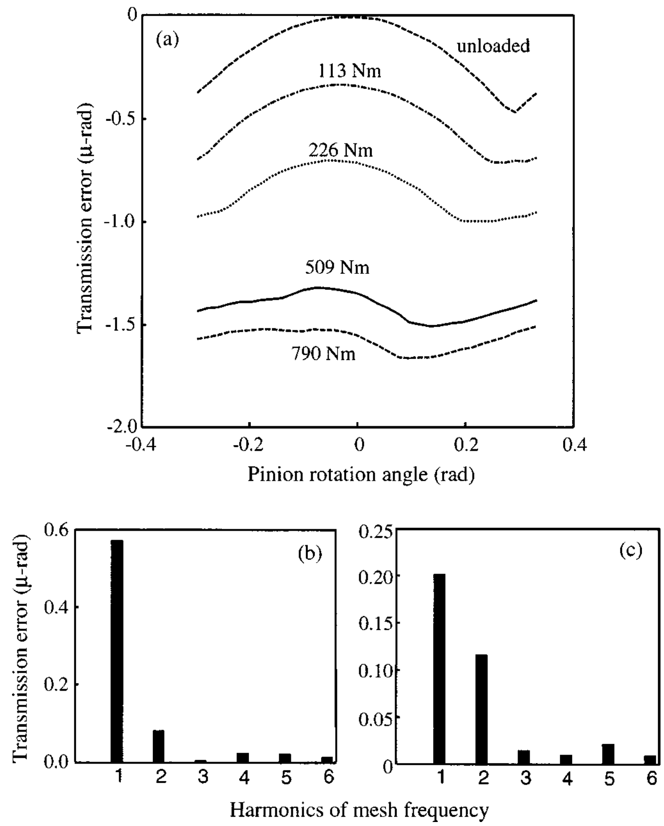

Fig. 4 Loaded transmission error and corresponding Fourier coefficients for two different pinion torques: (*a*) effect of load; (*b*) 113 Nm; and (*c*) 509 Nm

gear example, the largest degree of variations occurs around -10^0 and 8^0 of pinion roll angles shown in Fig. 7. It is this time-varying mesh characteristic that makes hypoid gear engagement unique, since it affects the instantaneous dynamic forces and moments acting on the pinion and gear. To understand the implications on the hypoid geared rotor system, the nonlinear time-varying (NLTV) model given by Eq. (8) is studied numerically as described earlier by applying the 5/6th order Runge-Kutta integration routine. In the analysis, the mesh force and bearing forces under steady state condition are predicted and compared to calculations for the time-invariant mesh cases. Figure 8 shows the predicted dynamic mesh loads in time domain over one mesh cycle using both the time-varying and time-invariant mesh vector models. The calculations are made at the response frequency of 340 Hz ($r=3$). The corresponding FFT spectra of both time responses are shown in Fig. 9. Figure 10 shows the dynamic mesh force and bearing force spectra predicted using the non-linear time-varying

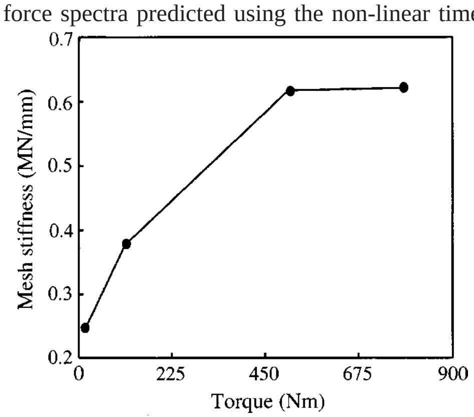

Fig. 5 Effect of mean pinion torque load on averaged mesh stiffness

Table 2 Classification of normal modes of the linear time-invariant system

Mode Description	Primary Modal Coordinates	Natural Frequency (Hz)		
		113 Nm	226 Nm	509 Nm
In-phase torsion and translation	2 $(Y_1-Y_2-\theta_E)$	222.4	222.6	222.2
Pure translation	5 (Z_2)	427.4	427.4	427.4
	8 (X_1)	887.9	887.9	887.9
Out-of-phase torsion and translation	1 $(Y_1-Y_2-\theta_E)$	204.1	205.1	205.2
	3 $(Y_1-X_2-Z_2-\theta_E-\theta_O)$	342.7	344.2	344.4
	4 $(Y_1-X_2-Z_2-\theta_O)$	391.2	391.3	391.3
	6 $(Y_1-X_2-Z_2-\theta_O)$	436.6	436.6	436.5
	7 $(Z_1-Y_1-X_2-Z_2)$	786.0	797.0	799.7
	9 (Z_1-Y_1)	1450.0	1704.4	1799.1

(NLTV) and time-invariant (NLTI) mesh vectors under relatively high pinion torque. Note that no tooth separation is seen in these cases. The response of the linear time-invariant (LTI) model is also shown for reference. The predicted responses of the nonlinear system are generally larger than the linear time-invariant levels. Also, the time-varying mesh model again produces slightly higher response amplitude than the time-invariant one in spite of the nonlinearity present, especially at lower frequencies ($\leqslant$400 Hz), which is consistent with the results of Figs. 8 and 9. The resonant peaks seen in the predicted response are related to $r=1$, $r=3$ and $r=7$ as defined in Table 2, which are essentially members of the family of modes with out-of-phase torsion coupled with translation motions. In addition to these primary resonances, numerous occurrences of super-harmonic response that are excited by higher order terms of LTE can be clearly visible for both the nonlinear time-varying (NLTV) and time-invariant (NLTI) simulation results. For instance, the resonance peak at around $f_m=900$ Hz in Fig. 10 is the super-harmonic of the ninth mode, i.e., $f_9/2$, which is excited by the second harmonic of LTE. Note that these super-harmonic excitations are not seen in the LTI calculations. Also, the fact that the super-harmonics are also present in the constant mesh stiffness case of the NLTI model excludes the possibility of the effects of higher order of k_m [17].

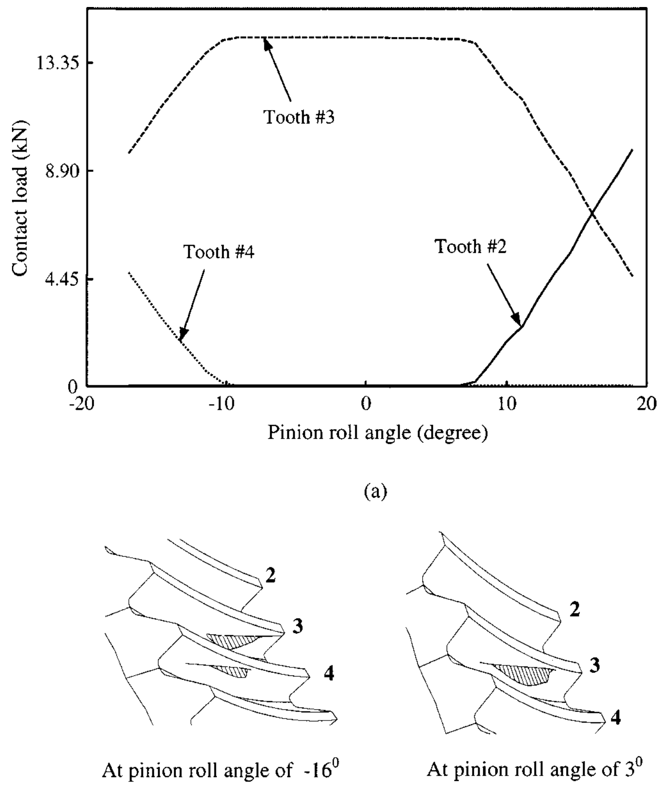

Fig. 7 Quasi-static multi-tooth contact analysis results of (*a*) load sharing characteristic within one mesh cycle at 509 Nm pinion input torque; and (*b*) load distributions for two different mesh positions

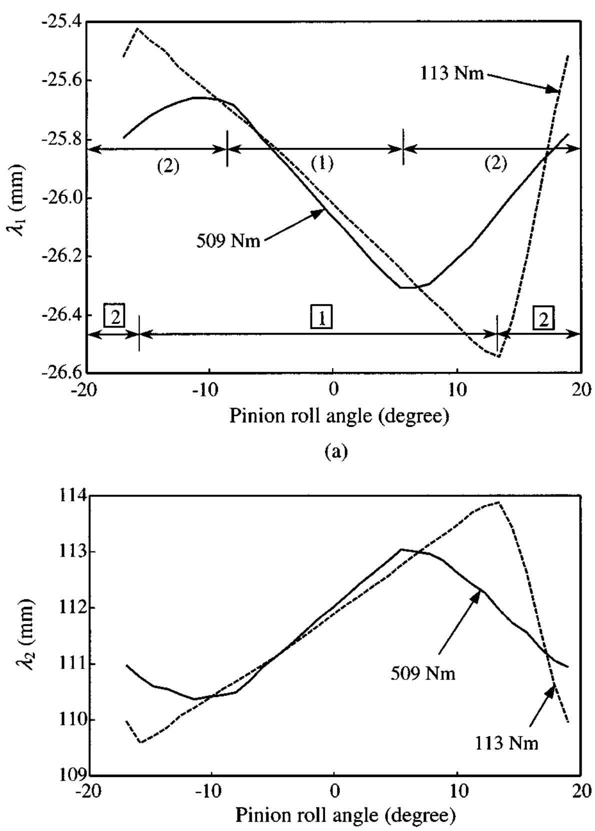

Fig. 6 Directional rotation radii (mm) corresponding to the equivalent quasi-static normal force under forward drive operating condition. The number of tooth pairs in contact is shown for the two torque loads at 113 Nm, $\boxed{\#}$, --------- ; and 509 Nm, (#),——.(*a*) Pinion; (*b*) Gear

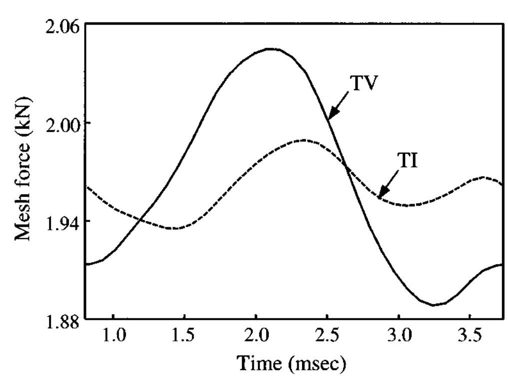

Fig. 8 Predicted dynamic mesh loads for one mesh cycle at the resonant frequency of 340 Hz for the case of time-varying (TV) and time-invariant (TI) mesh vectors at 509 Nm of applied pinion torque load (friction coefficient $\mu=0$)

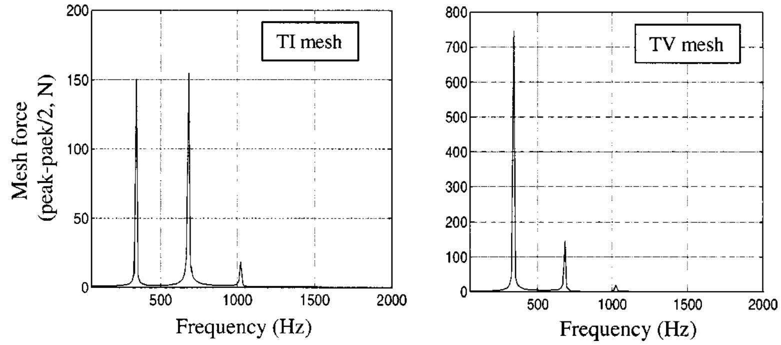

Fig. 9 Mesh load FFT spectra of the time response shown in Fig. 8

It is generally known that any particular tooth modification is aimed to reduce gear noise excitation for a certain operating load range [27–29]. Accordingly, the forced responses for several applied mean torque load cases are analyzed. Figure 11 shows the dynamic mesh force responses of low (113 Nm), medium (509 Nm) and high (790 Nm) input torques at the pinion using the same mesh stiffness to investigate the direct effect of transmission error. The dynamic response of the lighter torque load condition that corresponds to higher magnitude of transmission error, as shown in Fig. 4, is higher than that of the heavier torque load condition. However, if the effect of load on mesh stiffness, as illustrated in Fig. 5 is included in the simulation, we get the forced responses given by Figs. 12 and 13 for the dynamic mesh and pinion bearing forces respectively. Compared to the results of Fig. 11, we can see that the inclusion of the effect of changing mesh stiffness due to variation in transmitted load does not imply larger amplitude of dynamic response in the lighter torque load case relative to the higher torque ones in spite of its larger transmission error. Under light load condition (113 Nm), tooth separation is seen near 1250 Hz. This produces the classical jump phenomenon where the frequency response is discontinuous in the vicinity of the resonant frequency. In this case, it is noted that the full upper branch was produced by decreasing the rotational speed of the drive train, while the complete lower branch was formed by slowly increasing the rotational speed. This form of nonlinear behavior depicted is analogous to the classical softening spring case. Figure 14 shows the time history response functions of the dynamic mesh force before and after the jump frequency. Notice the vanishing tooth load when separation occurs; however no back-collision is observed.

On the other hand, tooth separation is not seen at all for higher input torque loads of 509 and 790 Nm. In these cases, the gear pairs in mesh maintain continuous contact, in spite of the backlash present. One of possible reasons that tooth separation occurs only at light torque load condition rather than heavier load case is because of its larger LTE excitation. In addition, the resonant peak frequencies tend to shift lower as load decreases due to the lower averaged mesh stiffness as pointed out previously. Further examination of the frequency response functions of the dynamic mesh force and bearing force, shown by Figs. 12 and 13 respectively, reveals some differences in the participating modes. For example, the dynamic mesh force response possesses a strong resonance

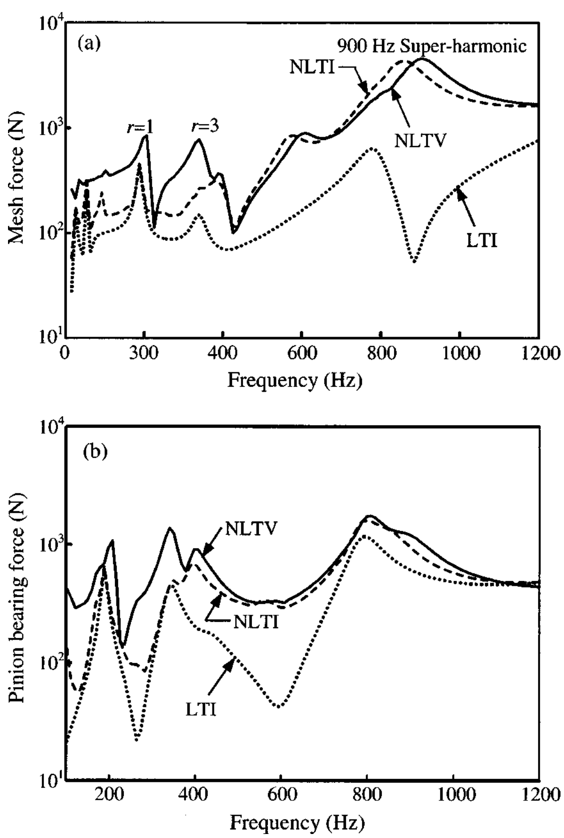

Fig. 10 Comparison of the frequency response functions of the non-linear time-varying (NLTV) and time invariant (NLTI) cases for 509 Nm of pinion torque. Note that the linear time-invariant response (LTI) is also plotted (friction coefficient $\mu = 0$)

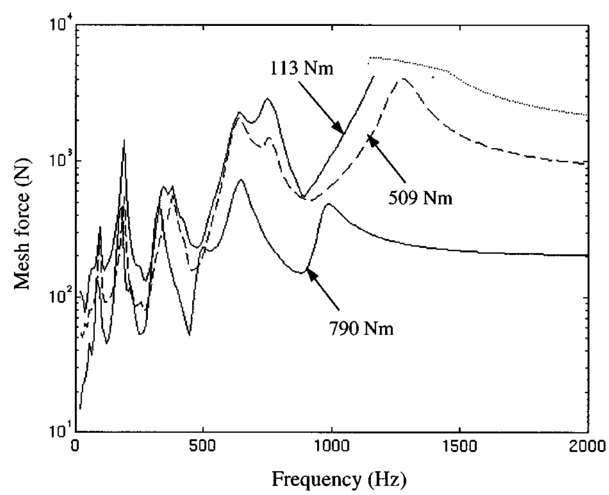

Fig. 11 Effect of applied pinion torque load on the dynamic mesh force assuming the same mesh stiffness of 3×10^8 N/m for all 3 cases shown (friction coefficient $\mu = 0$)

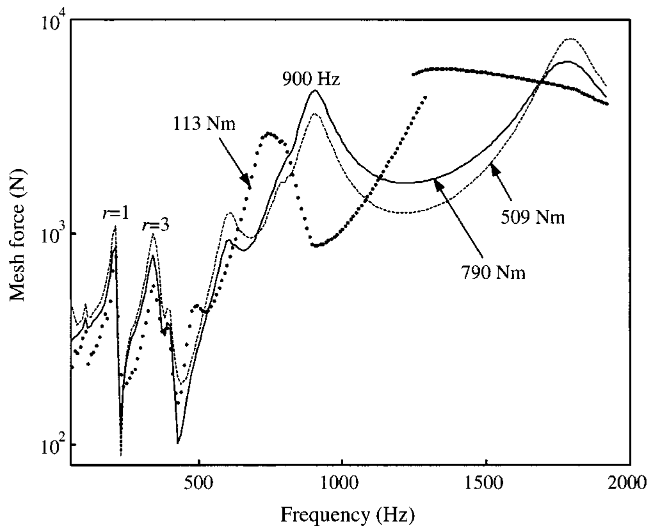

Fig. 12 Effect of applied pinion torque load on dynamic mesh force with load-dependent averaged mesh stiffness (no friction effect)

peak at mesh frequency of $f_m = 900$ Hz for the case 509 Nm torque load, which is missing from the bearing force response function. This peak response is in fact the super-harmonic of the 9th mode as seen earlier in Fig. 10. For torque load of 790 Nm, this peak is barely visible in the bearing force response even though it appears very strong in the dynamic mesh force. The differences observed are primarily due to the effect of dynamic transmissibility between the mesh and bearing support area. Alternatively, we observe a resonance peak at the lower 800 Hz corresponding to the primary excitation of mode 7. To explain this phenomenon quantitatively, the following two cases are simulated. The first case assumes a sinusoidal LTE at the fundamental mesh harmonic, while the second analysis uses the first three harmonics of LTE. Both calculations are performed by setting the mesh stiffness constant. However, the mesh vector (line-of-action) remains time-varying. The dynamic mesh force response spectra are shown in Fig. 15(*a*). Here, the fundamental harmonic of LTE clearly excites mode 7 ($f_7 = 799.7$ Hz), while the second harmonic of LTE provides excitation to mode 9 ($f_9 = 1799$ Hz) that shows up at $f_m = 900$ Hz. This is essentially at $f_9/2$ or 2 f_m super-harmonic frequency as described earlier. However, this is not seen

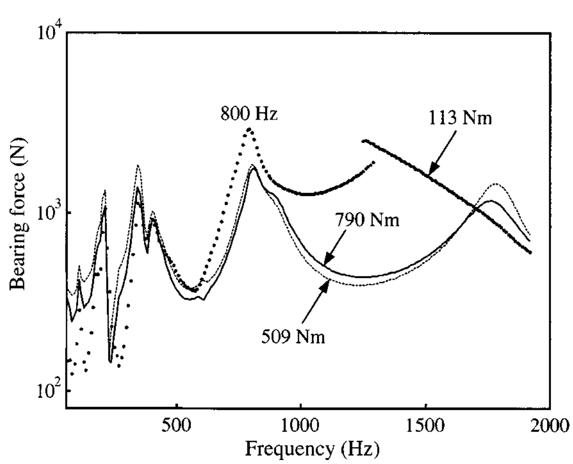

Fig. 13 Effect of applied pinion torque load on the pinion bearing force with load-dependent averaged mesh stiffness (no friction effect)

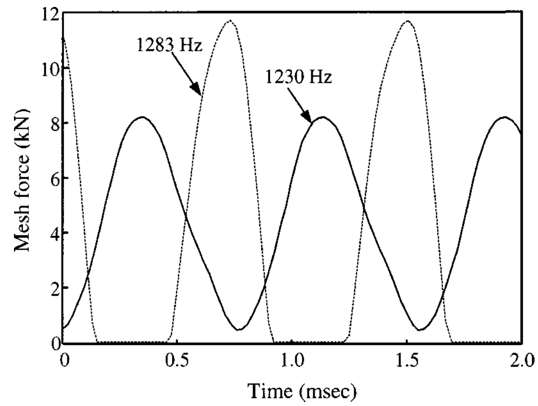

Fig. 14 Time-history response of the dynamic mesh force near the jump frequency under light load condition (113 Nm)

in the pinion bearing force response given by Fig. 15(*b*). These results also suggest that the commonly applied linear theory with only the fundamental harmonic of TE included would result in loss of super-harmonic effect.

The mean torque load effect on the dynamic transmission error for the cases of 113 and 226 Nm of pinion torques are shown in Fig. 16. The corresponding LTI solution is also shown for reference. Note that the jump frequencies are dependent on the torque load due to the changing averaged mesh stiffness. The primary resonant modes are 1, 3, 7 and 9, which are part of the modal family related to the gear out-of-phase torsion coupled with trans-

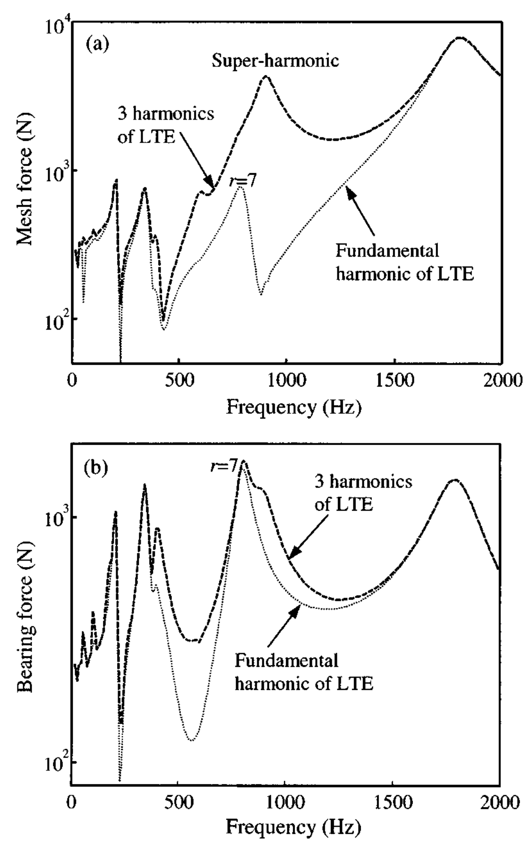

Fig. 15 Dynamic mesh force and pinion bearing force due to the fundamental harmonic of LTE compared to that of the first three harmonics of LTE. These cases assume 509 Nm of pinion torque, time-varying mesh vector, time-invariant mesh stiffness, and no friction effect.

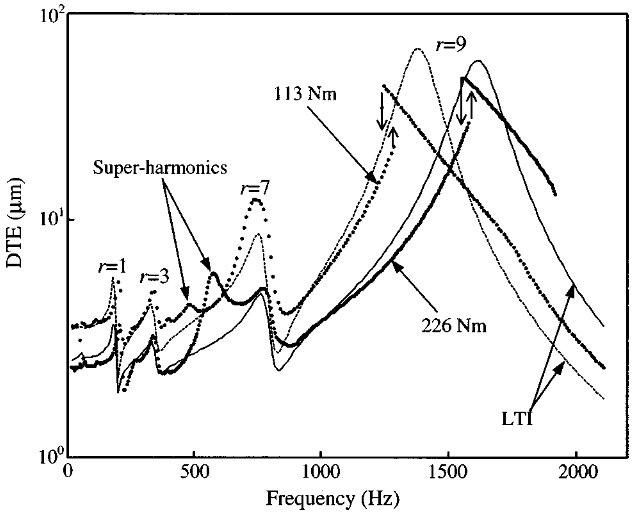

Fig. 16 Dynamic transmission error for 2 different pinion torque loads assuming constant mesh stiffness with time-varying mesh vector and no friction effect. The corresponding linear time-invariant solutions are also shown. The super-harmonics indicated are due to the 3rd harmonic of the LTE excitation.

lation motions. The resonances around 480 Hz for 113 Nm case and 580 Hz for 226 Nm case are not of the primary mode set, but super-harmonic response generated by the higher order excitations of LTE. To justify this observation, the FFT spectrum of the time trace response for the 226 Nm case is illustrated in Fig. 17. It shows that even though the system is being driven dynamically at $f_m = 580$ Hz, the response of the $3f_m$ harmonic component is also very high, since the third harmonic of LTE coincides exactly with the 9th mode.

Finally, the overall vibration of the system in frequency or mesh order domain is presented as 3-dimensional waterfall simulation of speed sweep plots. The Fourier Transform method is performed on the steady-state response at each speed to obtain the individual frequency content. This form of simulation can separate the net vibration levels into several mesh harmonics. Figure 18 shows the speed sweep waterfall plots of the dynamic pinion bearing force and mesh force responses for 509 Nm of input torque. One can see that the response peaks of the fundamental mesh

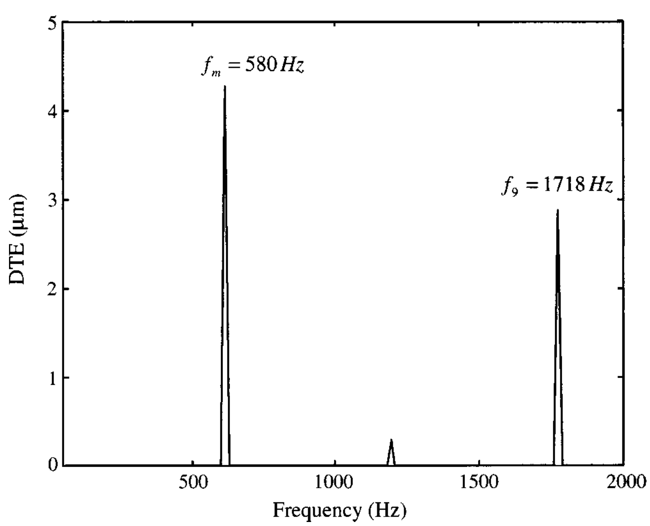

Fig. 17 Frequency spectrum of DTE (μm) at operating frequency of 580 Hz for the case of 226 Nm of input pinion torque

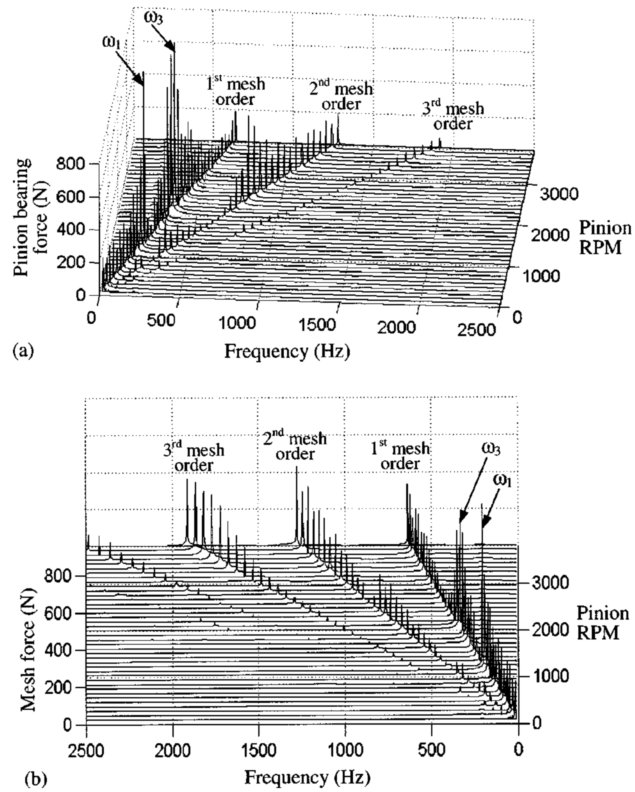

Fig. 18 Waterfall plots of the dynamic response at 509 Nm of input pinion torque. (*a*) Pinion bearing force; (*b*) Dynamic mesh force

order correspond to the damped resonant frequencies of the primary modes similar to the ones shown in lower frequency portion of Fig. 12. Also, the first harmonic is found to dominate the vibration spectra more than other higher harmonics especially at lower running speed where super-harmonics are much less significant. This is not the case at higher speeds where the second and third orders are just as significant as the fundamental one.

5 Summary

The present study presents a non-linear, time-varying, 3-dimensional gear mesh coupling characteristic for simulating the dynamics of hypoid gears, and includes the effect of backlash nonlinearity as well as time-dependent mesh position and line-of-action vectors. The time-varying mesh characteristic model is based on a 3-dimensional, quasi-static loaded tooth contact analysis. Coupled translation-torsion dynamic model of a generic hypoid geared rotor system is formulated employing the non-linear, time-varying mesh and is also studied numerically to predict the vibratory response due to loaded transmission error excitation. The resonant modes contributing to the response spectra are also identified, and cases with super-harmonics are illustrated. This study examines for the first time the effect of time-varying mesh vector on hypoid gear dynamics. Under light torque load condition, tooth separation is observed leading to the classical jump phenomenon.

Acknowledgments

The authors wish to express their appreciation to Professor Donald R. Houser at the Gear Dynamics and Gear Noise Research Laboratory at the Ohio State University for his constructive comments, and Dr. Sandeep Vijayakar at the Advanced Numerical Solutions Inc. for his guidance in the hypoid gear mesh generation work and his generosity for supplying the CAPP software. This material is based upon work partly supported by the National Science Foundation under Grant No. 9978581.

Nomenclature

c_{ij} = local compliance of contact cell ij
$[C_{lb}]$ = damping matrix
$[C_\delta]$ = compliance matrix of contact cells
e_0, e_{rc}, e_{rs} = Fourier terms of mean, cosine and sine parts of transmission error
e_L = loaded displacement transmission error
f = excitation frequency in Hz
f_m = gear mesh frequency in Hz
$\{\mathbf{E}_0\}$ = initial gear tooth separation vector
$\{\mathbf{F}_{ext}\}$ = external forcing vector
$\mathbf{g}$ = directional cosine vector of friction force
$\mathbf{h}$ = directional cosine vector of normal force
I = mass moment of inertia term
k = stiffness term
i,j,k = triad of unit vectors of a coordinate system
$[K]$ = stiffness matrix
m = mass term
$[M]$ = mass matrix
$[M_{l0}]$ = coordinate transformation matrix between S_l and S_0
$\mathbf{n}$ = surface normal vector
N_c = total number of contact cells
$\mathbf{q}_l$ = displacement vector of pinion ($l=1$) or gear ($l=2$)
r = mode number
$\mathbf{r}_i$ = position vector of contact cell i
S_l = coordinate systems
t = time (sec)
T_l = torques on pinion ($l=1$) and gear ($l=2$)
ν_{lj} = component of friction force vector ($j=x,y,z$)
W_0 = equivalent normal tooth load
x,y,z = translation coordinates
ε_0 = unloaded kinematic transmission error
δ_d = dynamic displacement transmission error
δ_j = deformation of contact cell j
$\Delta\theta_L$ = loaded angular transmission error
$[\Phi]$ = mode shape matrix
λ_u = directional rotation radius of normal force about the u-axis, $u=x,y,z$
μ = friction coefficient
θ_x, θ_y, θ_z = rotational coordinates
τ_u = directional rotational radius of friction force about the u-axis, $u=x,y,z$
θ_E = torsional coordinate of driver
θ_O = torsional coordinate of load
ω = excitation frequency in rad/sec
ω_m = gear mesh frequency in rad/sec

References

[1] Litvin, F. L., and Gutman, Y., 1981, ‘‘Method of Synthesis and Analysis for Hypoid Gear-drives of Format and Helixform,’’ ASME J. Mech. Des., **103**, pp. 83–113.
[2] Litvin, F. L., and Zhang, Y., 1991, ‘‘Local Synthesis and Tooth Contact Analysis of Face-milled Spiral Bevel Gear,’’ NASA Technical Report 4342 (AVSCOM 90-C-028).
[3] Litvin, F. L., Wang, A. G., and Handschuh, R. F., 1998, ‘‘Computerized Generation and Simulation of Meshing and Contact of Spiral Bevel Gears with Improved Geometry,’’ Comput. Methods Appl. Mech. Eng., **158**, pp. 35–64.
[4] Gosselin, C., Cloutier, L., and Sankar, S., 1989, ‘‘Effects of the Machine Settings on the Transmission Error of Spiral Bevel Gears Cut by the Gleason Method,’’ *Proc. International Power Transmission and Gearing Conference: New Technologies for Power Transmissions of the 90's*, Chicago, Illinois, pp. 705–712.
[5] Fong, Z. H., and Tsay, C. B., 1992, ‘‘Kinematical Optimization of Spiral Bevel Gears,’’ ASME J. Mech. Des., **114**, pp. 498–506.
[6] Kubo, A., Tarutani, I., Gosselin, C., Nonaka, T., Aoyama, N., and Wang, Z., 1997, ‘‘Computer Based Approach for Evaluation of Operating Performances of Bevel and Hypoid Gears,’’ JSME Int. J., Ser. III, **40**, pp. 749–758.
[7] Remmers, E. P., 1971, ‘‘Dynamics of Automotive Rear Axle Gear Noise,’’ SAE Paper 710114.
[8] Pitts, L. S., 1972, ‘‘Bevel and Hypoid Gear Noise Reduction,’’ SAE Paper 720734.
[9] Kiyono, S., Fujii, Y., and Suzuki, Y., 1981, ‘‘Analysis of Vibration of Bevel Gears,’’ Bull. JSME, **24**, pp. 441–446.
[10] Nakayashiki, A., 1983, ‘‘One Approach on the Axle Gear Noise Generated from the Torsional Vibration,’’ *Proc. Japanese Society of Automotive Engineers*, P-139, **2**, Tokyo, Japan, pp. 571–580.
[11] Abe, E., and Hagiwara, H., 1990, ‘‘Advanced Method for Reduction in Axle Gear Noise,’’ *Gear Design, Manufacturing and Inspection Manual*, Society of Automotive Engineers, Warrendale, PA, pp. 223–236.
[12] Özgüven, H. N., and Houser, D. R., 1988, ‘‘Mathematical Models Used in Gear Dynamic-a Review,’’ J. Sound Vib., **121**(3), pp. 383–411.
[13] Özgüven, H. N., and Houser, D. R., 1988, ‘‘Dynamic Analysis of High Speed Gears By Using Loaded Static Transmission Error,’’ J. Sound Vib., **125**, pp. 71–83.
[14] Kahraman, A., and Singh, R., 1990, ‘‘Non-linear Dynamics of a Spur Gear Pair,’’ J. Sound Vib., **142**(1), pp. 49–75.
[15] Kahraman, A., and Singh, R., 1991, ‘‘Non-linear Dynamics of a Geared Rotor-Bearing System With Multiple Clearances,’’ J. Sound Vib., **144**(3), pp. 469–505.
[16] Kahraman, A., and Singh, R., 1991, ‘‘Interactions Between Time-varying Mesh Stiffness and Clearance Non-linearities in a Geared System,’’ J. Sound Vib., **146**(1), pp. 135–156.
[17] Blankenship, G. W., and Kahraman, A., 1996, ‘‘Torsional Gear Pair Dynamics, Part-I: Characterization of Forced Response,’’ *Proc. International Power Transmission and Gearing Conference*, ASME, San Diego, CA **DE-88**, pp. 373–380.
[18] Blankenship, G. W., and Singh, R., 1995, ‘‘Dynamic Force Transmissibility in Helical Gear Pairs,’’ Mech. Mach. Theory, **30**, pp. 323–339.
[19] Velex, P., and Maatar, M., 1996, ‘‘A Mathematical Model For Analyzing The Influence of Shape Deviations and Mounting Errors on Gear Dynamic Behavior,’’ J. Sound Vib., **191**(5), pp. 629–660.
[20] Donley, M. G., Lim, T. C., and Steyer, G. C., 1992, ‘‘Dynamic Analysis of Automotive Gearing Systems,’’ Journal of Passenger Cars, **101**(6), pp. 77–87.
[21] Cheng, Y., and Lim, T. C., 1998, ‘‘Dynamic Analysis of High Speed Hypoid Gears With Emphasis on Automotive Axle Noise Problem,’’ *Proc. 7th International Power Transmission and Gearing Conference*, ASME, Atlanta, Georgia, DETC98/PTG-5784.
[22] Cheng, Y., and Lim, T. C., 2000, ‘‘Hypoid Gear Transmission with Non-linear Time-varying Mesh,’’ *Proc. 8th International Power Transmission and Gearing Conference*, ASME, Baltimore, Maryland, DETC2000/PTG-14432.
[23] Cheng, Y., and Lim, T. C., 2001, ‘‘Vibration Analysis of Hypoid Transmissions Applying an Exact Geometry-based Gear Mesh Theory,’’ J. Sound Vib., **240**(3), pp. 519–543.
[24] Hochmann, D., 1997, ‘‘Friction Force Excitation in Spur and Helical Involute Parallel Axis Gearing,’’ Ph.D. thesis, The Ohio State University, Columbus, Ohio.
[25] Lida, H., Tamura, A., and Yamada, Y., 1985, ‘‘Vibrational Characteristics of Friction Between Gear Teeth,’’ Bull. JSME, **28**(241), pp. 1512–1519.
[26] Handschuh, R. F., and Kicher, T. P., 1996, ‘‘A Method for Thermal Analysis of Spiral Bevel Gears,’’ ASME J. Mech. Des., **118**, pp. 580–585.
[27] Gosselin, C., Cloutier, L., and Nguyen, Q. D., 1995, ‘‘A General Formulation For the Calculation of the Load Sharing and Transmission Error Under Load of Spiral Bevel and Hypoid Gears,’’ Mech. Mach. Theory, **30**, pp. 433–450.
[28] Tavakoli, M. S., and Houser, D. R., 1986, ‘‘Optimum Profile Modifications for the Minimization of Static Transmission Errors of Spur Gears,’’ ASME J. Mech. Des., **108**, pp. 86–94.
[29] Krenzer, T. J., 1981, ‘‘Tooth Contact Analysis of Spiral Bevel and Hypoid Gears Under Load,’’ SAE Paper 810688.
[30] Vijayakar, S., 1987, ‘‘Finite Element Methods for Quasi-prismatic Bodies With Application To Gears,’’ Ph.D thesis, The Ohio State University, Columbus, Ohio.
[31] Vijayakar, S., 1991, ‘‘A Combined Surface Integral and Finite Element Solution for a Three-Dimensional Contact Problem,’’ Int. J. Numer. Methods Eng., **31**, pp. 525–545.
[32] Lim, T. C., and Singh, R., 1990, ‘‘Vibration Transmission Through Rolling Element Bearings. Part I: Bearing Stiffness Formulation,’’ J. Sound Vib., **139**(2), pp. 179–199.
[33] Lim, T. C., and Cheng, Y., 1999, ‘‘A Theoretical Study of the Effect of Pinion Offset on the Dynamics of Hypoid Geared Rotor System,’’ ASME J. Mech. Des., **121**, pp. 594–601.